ACS APPLIED MATERIALS & INTERFACES

www.acsami.org Research Article

Wide-Field Magnetic Field and Temperature Imaging Using Nanoscale Quantum Sensors

Christopher Foy, Lenan Zhang, Matthew E. Trusheim, Kevin R. Bagnall, Michael Walsh, Evelyn N. Wang, and Dirk R. Englund*

Cite This: *ACS Appl. Mater. Interfaces* 2020, 12, 26525−26533 Read Online

ACCESS | Metrics & More | Article Recommendations | Supporting Information

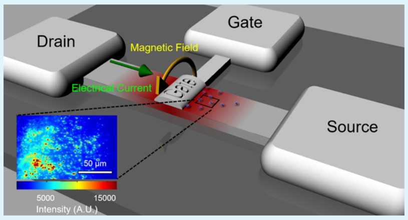

ABSTRACT: The simultaneous imaging of magnetic fields and temperature (MT) is important in a range of applications, including studies of carrier transport and semiconductor device characterization. Techniques exist for separately measuring temperature (e.g., infrared (IR) microscopy, micro-Raman spectroscopy, and thermo-reflectance microscopy) and magnetic fields (e.g., scanning probe magnetic force microscopy and superconducting quantum interference devices). However, these techniques cannot measure magnetic fields and temperature simultaneously. Here, we use the exceptional temperature and magnetic field sensitivity of nitrogen vacancy (NV) spins in conformally coated nanodiamonds to realize simultaneous wide-field MT imaging at the device level. Our "quantum conformally attached thermo-magnetic" (Q-CAT) imaging enables (i) wide-field, high-frame rate imaging (100−1000 Hz); (ii) high sensitivity; and (iii) compatibility with standard microscopes. We apply this technique to study the industrially important problem of characterizing multifinger gallium nitride high-electron mobility transistors (GaN HEMTs). We spatially and temporally resolve the electric current distribution and resulting temperature rise, elucidating functional device behavior at the microscopic level. The general applicability of Q-CAT imaging serves as an important tool for understanding complex MT phenomena in material science, device physics, and related fields.

KEYWORDS: *color center in diamond, nanodiamond, electronic devices, AlGaN/GaN HEMT, nitrogen vacancy, magnetic and temperature imaging, quantum sensing, electromigration*

1. INTRODUCTION

Magnetic field and temperature (MT) imaging play an important role in device-level characterization. The current density distribution determined through magnetic-field imaging provides valuable insight into the electronic performance and serves as a diagnostic tool to probe for current leakage or short circuits in the device,[1] whereas the temperature distribution elucidates the device thermophysical properties and heat transport.[2] For this reason, an imaging approach that combines magnetic field and temperature maps provides valuable information for model development and device performance optimization.

The need for MT imaging is one of the key drivers for the immense interest in ambient quantum sensing spin systems. In particular, the nitrogen vacancy (NV) center in diamond has attracted great interest because of its exceptional spin properties at room temperature, which exhibit outstanding nanoscale sensitivity to magnetic fields[3−8] and temperature.[9,10] NV centers located within nanodiamonds (NVNDs) have gained particular interest for applications including drug delivery,[11] thermal measurements of biological systems,[12−16] and scanning magnetometer tips.[17,18] The NVND's small size allows direct measurement of their local MT environment. These applications have motivated studies of NVND properties such as strain, magnetic and thermal sensitivity, and coherence time.[19,20] However, NVND properties differ for a given fabrication process[19] or surface treatment.[21] This variability of nanodiamond material parameters and orientations has presented challenges for wide-field imaging studies using NVNDs; simultaneous MT imaging at the electronic device level remains limited to date.

In this work, we (i) apply the models shown in the following works[22,23] to describe the optically detected magnetic resonance (ODMR)[24,25] spectrum of NVND ensembles as a function of magnetic field and temperature; (ii) perform statistical characterization of NVND parameters, specifically the variation in NVND thermal response with implications for NVND temperature sensing; (iii) use this NVND model and our statistical characterization to enable wide-field imaging with deposited coatings of NVNDs (Q-CAT imaging); (iv) demonstrate our technique's capabilities by imaging the dynamic phenomenon of electromigration; and (v) perform wide-field MT imaging of nontrivial commercial multifinger

Received: January 26, 2020
Accepted: April 23, 2020
Published: April 23, 2020

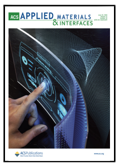

https://dx.doi.org/10.1021/acsami.0c01545
ACS Appl. Mater. Interfaces 2020, 12, 26525−26533

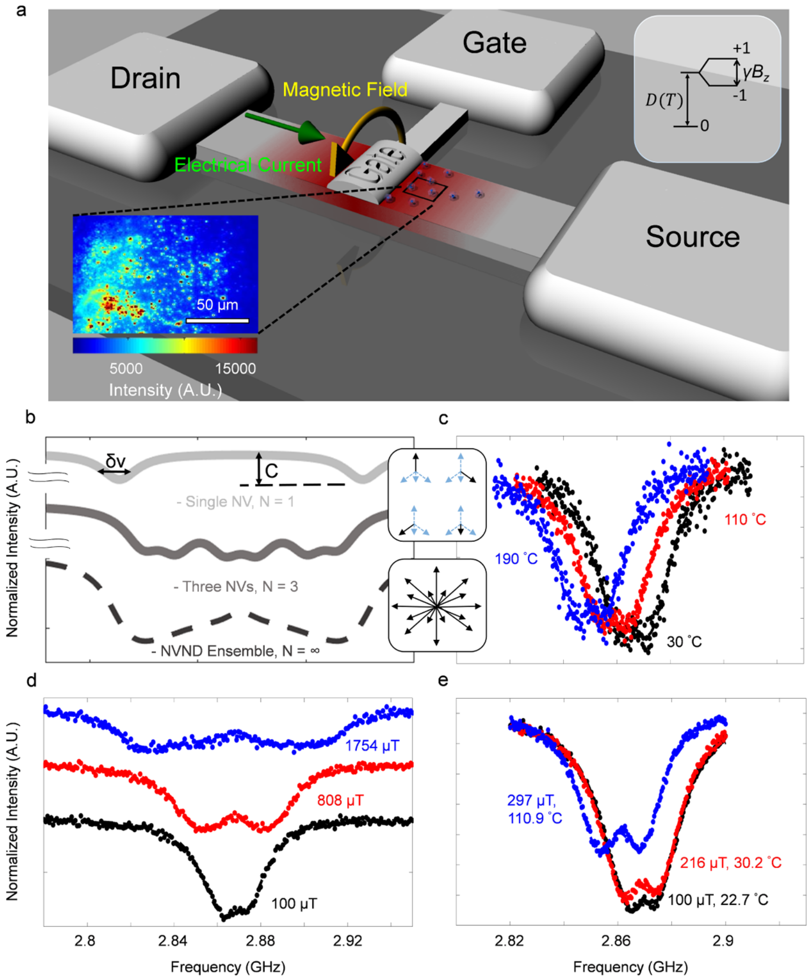

Figure 1. Overview of Q-CAT imaging. (a) Illustration of an application of Q-CAT imaging. A transistor experiences joule heating from electric current flowing between the drain and the source. (Inset bottom left) Fluorescence image of deposited NVNDs. NVNDs act as local probes of the magnetic field and temperature along the channel. (Inset top right) NV energy level diagram. (b) Simulated OMDR spectra for the case of 1,3 and infinite NVs within the diffraction limit for a given $|B|$. Resonance seen in the ODMR spectra change are resolvable at low N, but become inhomogeneously broadened as $N \to \infty$. (Inset) The top image shows NVs within defined crystallographic orientations such as those found in bulk diamond systems. The middle image shows 3 NV orientations constrained to the diamond crystallographic orientations. The bottom image represents NVs found in aggregated polycrystalline diamond. The NVs are modeled to be spherically symmetrical around an origin (bottom inset). (c) Increase in temperature shifts D to lower frequencies. (d) An increase in magnetic field broadens the ODMR curve. (e) The different responses of the NV ODMR spectrum to $|\vec{B}|$ and T allows for simultaneous measurements of the NVND's MT environment.

gallium nitride high-electron mobility transistors (GaN HEMTs) and characterize the electric current distribution and the resulting temperature rise.

2. SENSING WITH NVND ENSEMBLES

New diagnostic tools are needed to measure the MT profiles of microelectronics with high spatial and temporal resolution. For example, Figure 1a shows the temperature and magnetic field of a field-effect transistor. As the gate electrode modulates source-drain current, magnetic fields (gold arrow) and temperature (red surface) vary with a geometry-dependent spatial distribution. High current densities at the electronic junction lead to high temperatures that accelerate device degradation. While numerous temperature-mapping techniques are broadly used for characterization: infrared (IR) microscopy,[26] micro-Raman spectroscopy,[26] and thermo-reflectance microscopy,[26] each of these techniques has many undesirable features. IR and thermo-reflectance microscopy are both commonly used wide-field techniques but suffer from complicated calibration procedures and difficulties in measuring adjacent metal and semiconductor regions at the sample surface. Micro-Raman spectroscopy has the major advantage of directly probing the temperature in the active device layers but is limited to serial acquisition with a ∼1 μm diameter spot. Further, even if the temperature profile could be captured by the above techniques, the electric/magnetic current distribution would still not be understood or should be measured separately. A wide-field MT measurement technique with simple instrumentation and calibration procedures would therefore be of great value for electronics characterizations. To address these requirements we use a film of NVNDs for nanoscale spin-based magnetometry and thermometry, enabling Q-CAT imaging (Figure 1a inset). To generate images using Q-CAT imaging, we first determine the local magnetic field and temperature across a single NV by monitoring its average fluorescence intensity. In the $|m_s = 0\rangle$ "bright" state, the NV is photostable; in contrast, in the $|m_s = \pm 1\rangle$ state, the NV undergoes an intersystem crossing into a metastable state.[24,27] This decay path is nonradiative in the visible spectrum and thus reduces the NV's average fluorescence intensity. Fluctuations in the NV's local thermal environment change the $|m_s = 0\rangle \to |m_s =$

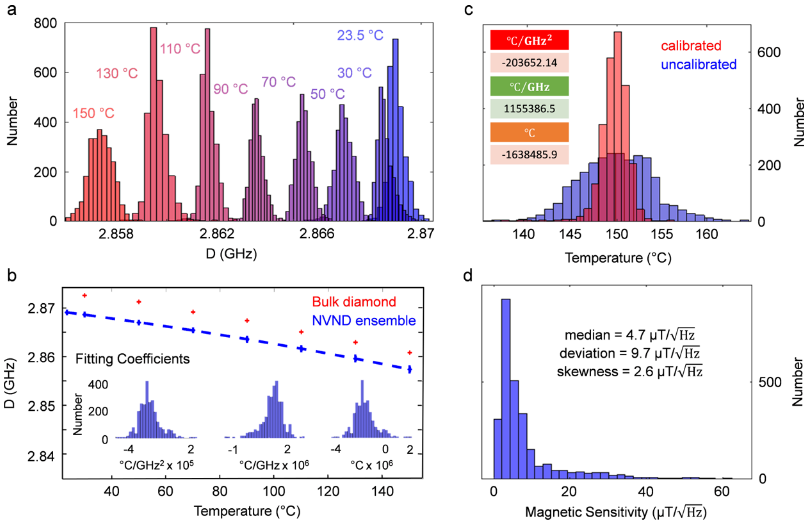

Figure 2. Statistical analysis of NVND properties. (a) Histograms of D as a function of T for NVND ensembles. (b) Fit of the mean value of D vs T. (Inset) Histogram of the fit coefficient. (c) Histogram of the measured temperature across all NVNDs using the average fit coefficients (uncalibrated) and individual fit coefficients for each NVND (calibrated). (d) Distribution of NVND magnetic sensitivity.

$\pm 1\rangle$ zero-field splitting parameter, $D(T)$,[28] whereas magnetic fields lift the degeneracy of the NV's $|m_s = \pm 1\rangle$ state through the Zeeman effect.[29] For weak nonaxial or aligned magnetic fields ($\vec{B} \approx B_z < 100$ mT), the resonance frequencies of the $|m_s = \pm 1\rangle$ states are given by[30]

$$\varepsilon(T, B_z)_{\pm} = D(T) \pm \sqrt{E^2 + (\gamma B_z)^2} \tag{1}$$

where $\epsilon_{\pm}$ are the NV resonance frequencies corresponding to the $|m_s = 0\rangle \rightarrow |m_s = \pm 1\rangle$ transitions, γ is the NV gyromagnetic ratio, E is the NV's off-axis zero-field splitting parameter,[30] which results from local strain, and B_z is the axial magnetic field. This behavior of the $|m_s = \pm 1\rangle$ states with magnetic field and temperature is represented graphically in Figure 1a inset top. We can measure $\epsilon_{\pm}$ through ODMR experiments (Figure 1b–e),[24] which allows us to determine $D(T)$ and B_z.

Figure 1b (top line) shows an ODMR spectrum of a single NV with an applied B_z. This spectrum has the form

$$I(f;\ \varepsilon,\ \delta\nu,\ C) = 1 - \sum_{m=1}^{2} L(f;\ \varepsilon_{\mathrm{m}},\ \delta\nu,\ C) \tag{2}$$

where $L(f; \epsilon, \delta\nu, C)$ is the three-parameter Lorentzian function, f is the microwave frequency, $\delta\nu$ is the linewidth of the transition, and C is the change in fluorescence rate between the $|m_s = 0\rangle$ and $|m_s = \pm 1\rangle$ states.

As the number of distinct NV center orientations, N, for a given B_z within a diffraction-limited volume increases, the final observed ODMR spectrum is the sum of the individual NV ODMR spectra having the form

$$I(f;\ \varepsilon,\ \delta\nu,\ C_{\mathrm{m}}) = 1 - (1/N)\sum_{i=1}^{N}\sum_{m=1}^{2} L(f;\ \varepsilon_{\mathrm{mi}},\ \delta\nu,\ C) \tag{3}$$

as seen in Figure 1b (middle line) for $N = 3$. NV centers located in single crystal bulk diamond can have at most four NV orientations,[31−34] belonging to the set shown in Figure 1 inset top, which lie along the diamond's [111] crystallographic axes.

For NVND ensembles, the number of possible NV orientations is not fixed.[35] As the number increases, NV resonances are no longer individually resolvable, as shown in Figure 1b (bottom line). To describe this behavior, we model the NVND ensemble as an isotropic distribution of NV orientations, each oriented at an angle $\theta \in [0, \pi]$ with respect to the objective axis (inset Figure 1b bottom). The ODMR spectrum becomes

$$\begin{aligned} &1 - I(f;\ T,\ |B|,\ \delta\nu,\ C) \\ &\quad \propto \int_0^{\pi} \sum_{m=1}^{2} R(\theta) L(f;\ \varepsilon(T,\ |B|)_{\mu\theta},\ \delta\nu,\ C) \sin\theta \ \mathrm{d}\theta \end{aligned} \tag{4}$$

where the summation becomes an integral, and $R(\theta)$ represents the angular-dependent weighting of the NV's normalized fluorescence value (see Supporting Information). The NVND ODMR spectrum as a function of magnetic field and temperature is shown in Figure 1c–e. Figure 1c illustrates how the center of the ODMR spectrum shifts to lower frequencies as its ambient temperature increases. Due to the isotropic model, NVNDs are insensitive to magnetic field orientation, so $B_z \rightarrow |\vec{B}|$. Figure 1d demonstrates how NVND ODMR spectra broaden as a function of $|B|$. Finally, Figure 1e shows $I(f; D(T), |B|, \delta\nu, C)$ for two values of $|B|$ and T (see Supporting Information for complete derivation). Fitting the measured spectra to eq 4 allows the determination of both $|B|$ and $D(T)$.

3. STATISTICAL CHARACTERIZATION OF NVND ENSEMBLES

Temperature imaging with NVNDs requires extracting T from $D(T)$. Thus, D as a function of temperature needs to be determined. Previous studies have investigated this dependence with limited numbers of NVNDs,[36] degrading the precision and accuracy of $D(T)$. In addition, NVNDs can have different $D(T)$, originating from varying nanodiamond impurity concentration, strain, and surface geometry.[28,37] To determine $D(T)$, we calibrate Q-CAT imaging with known temperatures. Importantly, the wide-field nature of Q-CAT imaging allows for the investigation of several hundreds of nanodiamonds in parallel—ideal for studying nanodiamond properties. This allows for determination of the NVND's $D(T)$ distribution.

https://dx.doi.org/10.1021/acsami.0c01545
ACS Appl. Mater. Interfaces 2020, 12, 26525−26533

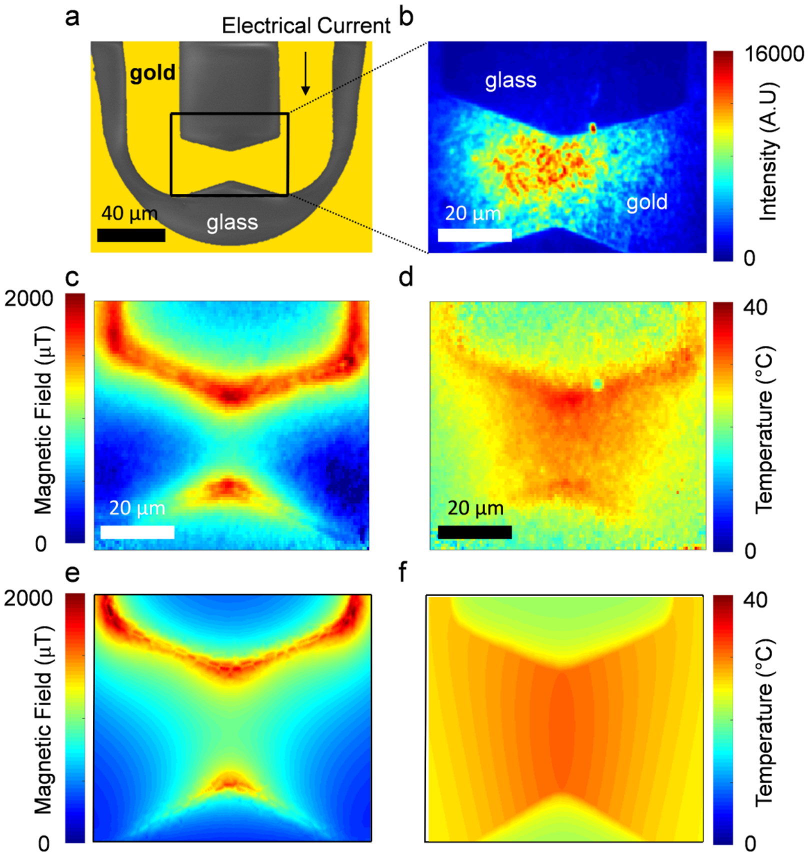

Figure 3. Q-CAT imaging of microfabricated structure. (a) False-color SEM of microfabricated structure to identify device structure. (b) Fluorescence image of deposited NVNDs. (c,d) Magnetic and temperature image of the ROI indicated in a. (e,f) MT simulations of the tapered region.

To determine D as a function of temperature, we tracked $D(T)$ across 2573 commercially available 100 nm CO−OH-terminated nanodiamonds (Adámas Nanotechnologies) from 23.5 to 150 °C (Figure 2a) using a temperature-controlled stage (see Methods). Figure 2b shows a second-order polynomial fit of the average NVND $D(T)$ compared with the measured $D(T)$ of bulk diamond NVs. NVND's D is lower than bulk diamonds across all temperatures, which we attribute to the nanodiamond's large strain ($E > 5$ MHz). Histograms of the distribution of fitting coefficients are within Figure 2b inset. We note that the mean measured standard deviation of the NVND thermal response across all temperatures (3.88 °C) is greater than what is expected from measurement error (2.17 °C ± 0.46 °C), indicating that individual NVNDs have varying thermal responses. This variation could result from differences in the thermal resistance at the nanodiamond sample interface, or, as previously theorized,[28] inherent variation in NVND thermal response. Figure 2c shows the distribution in the measured temperature using the mean value of the fitting coefficients-(Figure 2c inset). While individual NVNDs have shot-noise scaling in determining D at a particular temperature, Figure 2c demonstrates that the variation in thermal response among the NVND ensemble limits their temperature accuracy for imaging applications.

To compensate for the variation in $D(T)$, we apply the fitting coefficients in Figure 2b inset to each NVND. This individual NVND $D(T)$ calibration improves the mean temperature precision to 2.6 °C per pixel ($\sim 1\ \mu\text{m} \times 1\ \mu\text{m}$) across all NVNDs, which is within the variation expected from the experimental noise. These results suggest that improving the uniformity of $D(T)$ among NVNDs should be a priority for future nanodiamond fabrication studies. The precision of Q-CAT imaging is comparable to that of alternative thermal imaging techniques such as micro-Raman spectroscopy (1 °C)[26] and IR (1 °C).[26]

We also investigated the NVND's magnetic field sensitivity (Figure 2d) and measured a median of 4.7 $\mu\text{T}/\sqrt{\text{Hz}}$ (see Supporting Information). We measure a standard deviation of 9.7 $\mu\text{T}/\sqrt{\text{Hz}}$ and a skewness of 2.6 $\mu\text{T}/\sqrt{\text{Hz}}$. This distribution contains values ranging from 1.2 to 64.4 $\mu\text{T}/\sqrt{\text{Hz}}$. This range indicates that future studies on NVND sensitivity need to carefully consider NVND median sensitivity and the entire distribution in order to rigorously determine how changes to NVND surface chemistry[38] and fabrication affect performance.

4. DEMONSTRATING Q-CAT IMAGING

To demonstrate Q-CAT imaging, we image one of the simplest structures that couples electromagnetism and heat transport: a thin gold wire with a narrowed tapered region. Similar structures have been imagined previously;[39,40] however this demonstration is the first time NVNDs have been used to conduct wide-field MT imaging. Figure 3a is a scanning electron microscope (SEM) image of the test system. Electric current (30 mA) induces significant local joule heating around the tapered region (dashed black box). The surrounding metal structure supplies the resonant microwave field, which drives the NV's spin resonances. We deposit NVNDs on top of the structure (thickness ∼100 nm, see Supporting Information). This NVND coating solves two issues found with bulk diamond

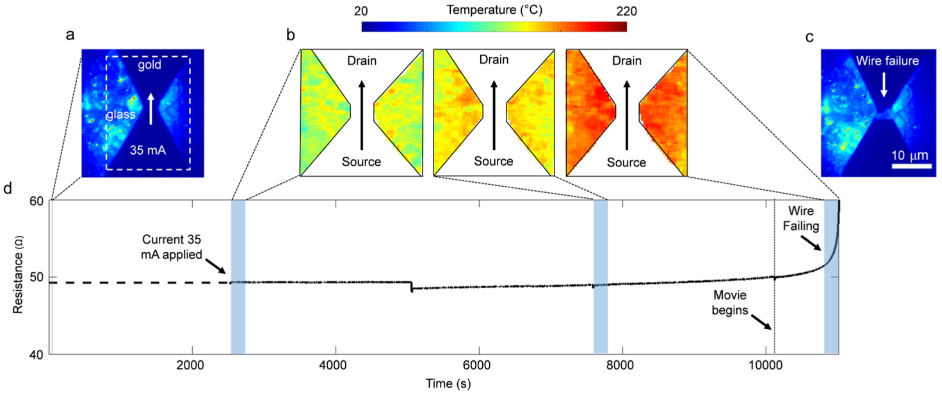

Figure 4. Q-CAT imaging of electromigration. (a) Fluorescence image of kinked wire after NVND deposition. (b) Temperature images of the wire, after 35 mA of current is applied, until wire failure. (c) Fluorescence image of wire after failure. (d) Resistance as a function of time. Resistance was determined by dividing the applied voltage by the current. Boxes represent measurement time for each image. The periodic jumps are artifacts that result from the experiment being suspended as the camera buffer is emptied. The dashed line is the extrapolated resistance before current was applied. The attached video's frame rate was artificially increased to shorten video time.

NV thermometry; due to the conformal coating it has good thermal contact with substrates (see Supporting Information) and avoids heat spreading because of the much lower thermal conductivity of diamond nanoparticles.[41] Both issues limit spatial resolution and artificially reduce peak temperature (see Supporting Information). An electron-multiplying charge-coupled device (EMCCD) camera images the NVND red fluorescence as shown in Figure 3b. Figure 3c,d shows images of the magnetic field and temperature of the tapered region, which are measured simultaneously by extracting $|B|$ and D from fits of the ODMR spectrum measured at each pixel. We determine temperature by converting D using the coefficients presented in Figure 2c inset. These images give insight into how the current flows through the structure, with a high magnetic field region at the structure's edge because the current density increases from both the structure's tapering and magnetic contributions from the side walls. We also see that the temperature is 10 °C higher at the kinked region, which indicates that this area is the probable point of failure for the device. Figure 3e,f shows MT (COMSOL) simulations of the taper region. We note strong agreement between measurements and simulations, and we attribute deviations from the simulations to the unknown fluctuations in the structure's surface morphology. According to this proof-of-concept study, two significant advantages of the proposed technique have been clearly shown. First, the electric/magnetic current distribution and the associated heating effect have been demonstrated at the wide field. Second, the microscale temperature distribution on the glass substrate, which has a weak thermo-reflectance and Raman signature, is well-resolved through Q-CAT imaging.

5. Q-CAT IMAGING OF DYNAMIC PROCESSES

While the previous experiment was at steady state, we also wish to showcase Q-CAT imaging of a dynamic process, which is difficult to capture with conventional techniques.[26] Thus, we apply Q-CAT imaging to study electromigration within microstructures. Electromigration is a runaway process, which concerns the failure of a conductor due to momentum transfer between the conducting electrons and the metal atoms, causing the metal ions to move and creating discontinuities. As we will show, a wide-field technique like Q-CAT imaging is well-suited to study this dynamic phenomenon because it allows high-frame rate MT imaging.

To begin the electromigration process, we increase the current through a similar kinked wire to a constant 35 mA and drive the device to failure. Figure 4a shows a fluorescence image of the structure at $t = 0$ s. Fluorescent areas are deposited NVNDs. Q-CAT imaging shows that the temperature increases over three distinct time intervals as the wire undergoes electromigration (Figure 4b). In the first shaded region, the device is still operating normally, and resistance is constant. In the second shaded interval, the resistance starts to linearly increase, and in the final region, failure is imminent and the resistance of the wire exponentially increases (Figure 4d). The local temperature increases over time from 50 to 220 °C. Within 10 ms of the final image shown in Figure 4b, the wire breaks and can no longer support electric current. Figure 4c shows a fluorescence image of the wire after failure with a tear at the kink, the location of temperature maximum, which is the point of failure of the device. The high temperature indicates the location of maximum electric current density and highest electron-gold momentum transfer—the source of electromigration. As expected, due to the constant current of 35 mA, the overall magnetic field distribution did not change over the course of the measurement. This process, beginning at the vertically dashed line, is shown in the attached video, which is sped up for ease of viewing.

The exposure time for each fluorescence image was 10 ms, with a total integration time of 100 ms per microwave frequency, corresponding to a total measurement time for each of the shaded intervals of ~48 s. However, 83% of the measurement time was occupied by camera readout time. In addition, the high count rate of the NVNDs ($<1 \times 10^7$ cps) coupled with the small electron well depth of our camera ($<80{,}000\ e^-$) limited the minimum exposure time. For a camera optimized for bright samples, the exposure time could be decreased further, by increasing the optical pump power. This limitation indicates that a frame rate of 100−1000 Hz is possible if a sparse sampling scheme was adopted (see Supporting Information) and the experimental overhead frame readout time (50 ms) was eliminated using a camera with integrate while read capabilities and high frame rates.[42] This frame rate compares favorably to *in situ* methods such as micro-Raman, which requires ~1 s per pixel, and is comparable to other wide-field techniques such as IR imaging or thermo-reflectance microscopy.

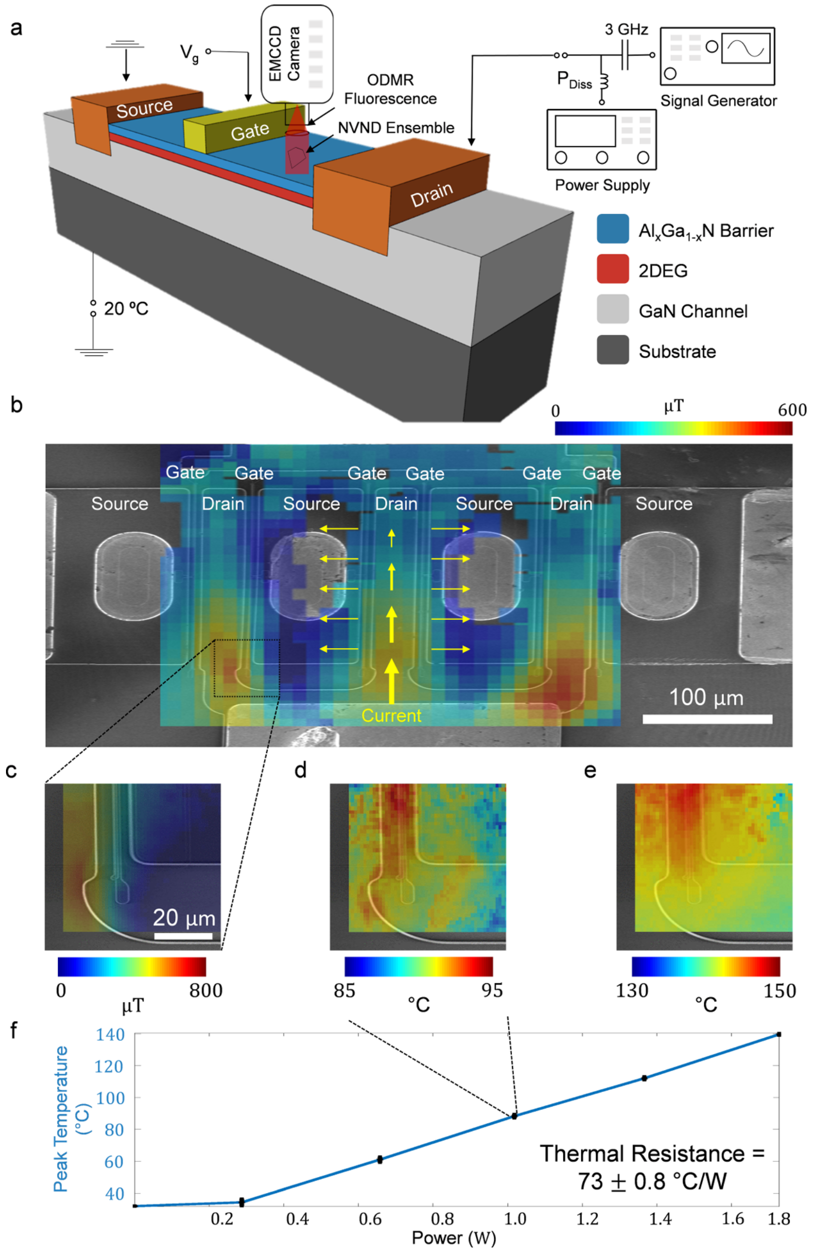

Figure 5. Q-CAT imaging of a multifinger GaN HEMT. (a) Schematic of Q-CAT imaging of a GaN HEMT. (b) Magnetic image of a six-finger GaN HEMT in the ON state (4 V, 72 mA). An SEM is superimposed to guide the eye. The magnetic field concentrates at the drain and decreases along the channel width. (c) High-resolution magnetic field (290 mW) and (d,e), temperature images of the channel stop (1 and 1.73 W respectively). (f) Peak temperature in the ON state as a function of the drain bias. We measure a thermal resistance of 73 ± 0.8 °C/W.

6. Q-CAT IMAGING OF GAN HEMTS

We further expand Q-CAT imaging beyond proof-of-principal experiments. We will image a technologically important problem where the interplay between temperature and electric currents is crucial and Q-CAT's wide-field MT imaging capability is essential—GaN HEMTs. GaN HEMTs are field-effect transistors which incorporate a junction between two materials with different band gaps. They are increasingly used in applications ranging from radio frequency amplifiers[43] to high power electronics.[44] The extremely high power density (>5 W/mm) in GaN HEMTs gives rise to a concentrated (∼1 μm) channel temperature (>200 °C), which leads to device failure.[45−48] The operation of GaN HEMTs involves nonlinear coupling between electromagnetism and heat transport, making their dynamics difficult to capture by simulation, especially when considering device variations. The problem is particularly challenging for the complex geometries of commercial, multifinger GaN HEMTs. We will image GaN's MT environment to both understand how current flows through the device and identify temperature maxima—the likely failure point, whose magnitude is predictive of device lifetime.

Figure 5a illustrates a GaN HEMT under Q-CAT imaging. The current, carried as a 2D electron gas (2DEG) from drain to source, is modulated by the top gate. Figure 5b shows the associated magnetic field for a commercial six-finger GaN HEMT superimposed over an SEM of the device. A power of 290 mW was applied across the drain while a gate voltage of −2.5 V (threshold voltage −2.8 V) was applied to keep the device in the ON state. The magnetic field decreases from the base of the drain by ~300 μT as the current drops along the channel width, as illustrated by the yellow arrows.

We sought to investigate the area with high magnetic field, the channel stop, and thus we conducted high-resolution (50×) MT imaging of that region (Figure 5c−e). As expected, the magnetic field of the left side of the channel stop is higher because the resistance of the GaN channel is much higher than that of the drain. The resulting temperature profile is obtained simultaneously. Significant temperature rise is localized around the gate, which agrees with previous experimental observations.[45−48] Particularly, attributed to the high spatial resolution and wide-field nature of Q-CAT imaging, a sharp temperature drop is well-resolved at the end of the gate along the channel direction (Figure 5d,e), indicating limited leakage current at the channel's end. Figure 5f shows the peak temperature as a function of dissipated power. We measure a thermal resistance of 73 ± 0.8 °C/W, which agrees with previous measurements of the same model (75 °C/W).[45] These results elucidate device physics at a spatial resolution that is competitive with *in situ* methods, at wide field.

7. CONCLUSIONS

Significant improvements in the sensitivity of Q-CAT imaging are possible. They could be achieved by NVNDs possessing coherence times approaching what has been demonstrated with bulk diamond.[19,49] Sensitivity could be further extended by using dynamical decoupling pulse sequences.[29] We estimate that mK/$\sqrt{\text{Hz}}$[12] temperature precision and sub nT/$\sqrt{\text{Hz}}$[49] magnetic field sensitivity are achievable with Q-CAT imaging. Q-CAT imaging has further advantages not demonstrated in this work. The unique method of NVND deposition enables the imaging of nonplanar geometries (see Supporting Information). Also, the temporal resolution of this technique could be extended for periodic signals through stroboscopic imaging, in which the laser readout for the NVNDs is pulsed in sync with the application of the electric current. In this manner, a temporal resolution of 10 ns could be achieved, which is limited by the laser gating time. This application could be of interest in studying the transient behavior of the MT environment of microelectronic devices, such as the peak temperature of GaN HEMTs at MHz frequencies.

In conclusion, Q-CAT imaging has a number of significant advantages: wide-field measurement with a field of view greater than 100 μm × 100 μm, compatibility with microscopes and almost all materials, and a mean thermal sensitivity comparable to micro-Raman spectroscopy and IR microscopy. Further, it has a diffraction limited spatial resolution (<1 μm). One possible shortcoming of Q-CAT imaging is that it requires samples that are resilient to microwave fields, which is common for most solid-state devices. In addition, because Q-CAT imaging is an optical measurement, it requires samples with low background red fluorescence ($<1 \times 10^6$ cps) under green excitation. We believe that these requirements are not especially restrictive for many active fields of research. Allowing, at a fundamental level, investigation of both steady state and transient thermal transport in a variety of materials systems and characterization of material thermophysical properties. At the device level, Q-CAT imaging helps understand the working principle, life-time, and failure mechanisms of devices. These applications are of interest to various fields such as microelectronics, ceramic memories, and lithium-ion batteries.

8. METHODS

8.1. Experimental Setup. A Verdi g2 532 nm single-mode longitudinal laser was focused through a custom microscope onto the back aperture of an objective. The resulting collimated excitation beam was used to pump the NVNDs. Emitted red fluorescence from the NVNDs was collected and measured using an Andor EMCCD camera. A 532 nm notch filter and 650 nm long pass were used to eliminate background fluorescence from the green excitation pump and the neutral charge state of the NV, respectively. The microwave excitation was swept by using a signal generator (Hewlett Packard ESG—D4000A). Collected fluorescence was correlated with microwave frequency in postprocessing to determine the ODMR spectra shown in the main text.

8.2. Microfabricated Structure Preparation. The sample shown in Figures 3 and 4 was fabricated in MIT's cleanroom facility, the Microsystems Technology Laboratory, using photolithography. We deposited a positive resist (S1813) onto a #1 glass coverslip and spun at 3 krpm for 1 min. The coverslips were exposed through a mask at 2100 μW/cm^2 for 40 s. Finally, they were developed in CD-26 for 15 s while stirring. Next, a titanium adhesion layer (20 nm) and a gold metallic layer (100, 50 nm respectively) were deposited. After deposition, acetone was used to strip the resist.

8.3. Temperature Setup. Temperature measurements of the NVND's thermal properties were conducted using a heating stage supplied by Instec Inc (HCP621 V) rated for a temperature precision of 50 mK.

8.4. GaN HEMT Preparation. GaN HEMTs were acquired from Wolfspeed/Cree (CGHV1J006D-GP4) and were mounted on custom PCBs. Gate and drain voltages were controlled through programmable power supplies, and a bias tee was used to feed in the 3 GHz frequency to drive the NV spins. A thermoelectric cooler mounted with a liquid cooling stage supplied by Koolance was used to cool the GaN HEMT backside to 20 °C during operation.

■ ASSOCIATED CONTENT

Supporting Information

The Supporting Information is available free of charge at https://pubs.acs.org/doi/10.1021/acsami.0c01545.

Video of NVND fluorescence as the wire undergoes electromigration (MP4)

Overview of the NV center, a detailed derivation of the QCAT fitting model, a breakdown in sources of measurement error, simulations showing the impact the deposited nanodiamond layer may have on the underlying thermal profile of our sample, sparse sampling protocol to increase the measurement rate, and finally SEMs of the samples both before and after the nanodiamonds were deposited (PDF)

■ AUTHOR INFORMATION

Corresponding Author

Dirk R. Englund − *Department of Electrical Engineering and Computer Science and Research Laboratory of Electronics (RLE), Massachusetts Institute of Technology, Cambridge, Massachusetts 02139, United States;* orcid.org/0000-0002-1043-3489; Email: englund@mit.edu

Authors

Christopher Foy − *Department of Electrical Engineering and Computer Science and Research Laboratory of Electronics (RLE), Massachusetts Institute of Technology, Cambridge, Massachusetts 02139, United States;* orcid.org/0000-0003-4872-6321

Lenan Zhang − *Department of Mechanical Engineering, Massachusetts Institute of Technology, Cambridge, Massachusetts 02139, United States;* orcid.org/0000-0002-8740-2736

Matthew E. Trusheim − *Department of Electrical Engineering and Computer Science and Research Laboratory of Electronics (RLE), Massachusetts Institute of Technology, Cambridge, Massachusetts 02139, United States*

Kevin R. Bagnall − *Department of Mechanical Engineering, Massachusetts Institute of Technology, Cambridge, Massachusetts 02139, United States*

Michael Walsh − *Department of Electrical Engineering and Computer Science and Research Laboratory of Electronics (RLE), Massachusetts Institute of Technology, Cambridge, Massachusetts 02139, United States*

Evelyn N. Wang − *Department of Mechanical Engineering, Massachusetts Institute of Technology, Cambridge, Massachusetts 02139, United States;* orcid.org/0000-0001-7045-1200

Complete contact information is available at:
https://pubs.acs.org/10.1021/acsami.0c01545

Notes

The authors declare no competing financial interest.
The data that support the findings of this study are available from the corresponding authors on reasonable request.

■ ACKNOWLEDGMENTS

This research is supported in part by the Army Research Office Multidisciplinary University Research Initiative (ARO MURI) biological transduction program. M.E.T. acknowledges support by an appointment to the Intelligence Community Postdoctoral Research Fellowship Program at MIT, administered by Oak Ridge Institute for Science and Education through an interagency agreement between the U.S. Department of Energy and the Office of the Director of National Intelligence. E.N.W., L.Z., and K.R.B. acknowledge funding support provided by the MIT/MTL GaN Energy Initiative and the Singapore-MIT Alliance for Research and Technology (SMART) LEES Program. K.R.B. also acknowledges that this research was conducted with government support under and awarded by DoD, Air Force Office of Scientific Research, National Defense Science and Engineering Graduate (NDSEG) Fellowship, 32 CFR 168a. M.W. was supported in part by the STC Center for Integrated Quantum Materials (CIQM), NSF Grant no. DMR-1231319, in part by the Army Research Laboratory Center for Distributed Quantum Information (CDQI). L.Z. also acknowledges the funding support provided by the Office of Naval Research (ONR) under Award no. N00014-17-1-2363. The authors would also like to thank Sinan Karaveli, Tim Schröder, Donggyu Kim, Alberto Lauri, Sara Mouradian, Eric Bersin, Kurt Broderick, and David Lewis for their helpful discussion.

■ REFERENCES

(1) Infante, F.; Perdu, P.; Petremont, S.; Lewis, D. A New Methodology for Short Circuit Localization on Integrated Circuits using Magnetic Microscopy Technique Coupled with Simulations. *16th IEEE International Symposium on the Physical and Failure Analysis of Integrated Circuits*, 2009; pp 208−212, ISSN: 1946-1550.

(2) Zhang, L.; Lu, Z.; Song, Y.; Zhao, L.; Bhatia, B.; Bagnall, K. R.; Wang, E. N. Thermal Expansion Coefficient of Monolayer Molybdenum Disulfide Using Micro-Raman Spectroscopy. *Nano Lett.* **2019**, *19*, 4745−4751.

(3) Maze, J. R.; Stanwix, P. L.; Hodges, J. S.; Hong, S.; Taylor, J. M.; Cappellaro, P.; Jiang, L.; Dutt, M. V. G.; Togan, E.; Zibrov, A. S.; Yacoby, A.; Walsworth, R. L.; Lukin, M. D. Nanoscale Magnetic Sensing With an Individual Electronic Spin in Diamond. *Nature* **2008**, *455*, 644−647.

(4) Balasubramanian, G.; Chan, I. Y.; Kolesov, R.; Al-Hmoud, M.; Tisler, J.; Shin, C.; Kim, C.; Wojcik, A.; Hemmer, P. R.; Krueger, A.; Hanke, T.; Leitenstorfer, A.; Bratschitsch, R.; Jelezko, F.; Wrachtrup, J. Nanoscale Imaging Magnetometry With Diamond Spins Under Ambient Conditions. *Nature* **2008**, *455*, 648−651.

(5) Grinolds, M. S.; Warner, M.; De Greve, K.; Dovzhenko, Y.; Thiel, L.; Walsworth, R. L.; Hong, S.; Maletinsky, P.; Yacoby, A. Subnanometre Resolution in Three-Dimensional Magnetic Resonance Imaging of Individual Dark Spins. *Nat. Nanotechnol.* **2014**, *9*, 279−284.

(6) Jensen, K.; Leefer, N.; Jarmola, A.; Dumeige, Y.; Acosta, V. M.; Kehayias, P.; Patton, B.; Budker, D. Cavity-Enhanced Room-Temperature Magnetometry Using Absorption by Nitrogen-Vacancy Centers in Diamond. *Phys. Rev. Lett.* **2014**, *112*, 160802.

(7) Glenn, D. R.; Lee, K.; Park, H.; Weissleder, R.; Yacoby, A.; Lukin, M. D.; Lee, H.; Walsworth, R. L.; Connolly, C. B. Single-Cell Magnetic Imaging using a Quantum Diamond Microscope. *Nat. Methods* **2015**, *12*, 736−738.

(8) Steinert, S.; Dolde, F.; Neumann, P.; Aird, A.; Naydenov, B.; Balasubramanian, G.; Jelezko, F.; Wrachtrup, J. High Sensitivity Magnetic Imaging Using an Array of Spins in Diamond. *Rev. Sci. Instrum.* **2010**, *81*, 043705.

(9) Neumann, P.; Jakobi, I.; Dolde, F.; Burk, C.; Reuter, R.; Waldherr, G.; Honert, J.; Wolf, T.; Brunner, A.; Shim, J. H.; Suter, D.; Sumiya, H.; Isoya, J.; Wrachtrup, J. High-Precision Nanoscale Temperature Sensing Using Single Defects in Diamond. *Nano Lett.* **2013**, *13*, 2738−2742.

(10) Laraoui, A.; Aycock-Rizzo, H.; Gao, Y.; Lu, X.; Riedo, E.; Meriles, C. A. Imaging Thermal Conductivity With Nanoscale Resolution Using a Scanning Spin Probe. *Nat. Commun.* **2015**, *6*, 8954.

(11) Perevedentseva, E.; Lin, Y.; Jani, M.; Cheng, C. Biomedical Applications of Nanodiamonds: Imaging and Therapy. *Nanomedicine* **2013**, *8*, 2041.

(12) Kucsko, G.; Maurer, P. C.; Yao, N. Y.; Kubo, M.; Noh, H. J.; Lo, P. K.; Park, H.; Lukin, M. D. Nanometre-Scale Thermometry in a Living Cell. *Nature* **2013**, *500*, 54−58.

(13) Simpson, D. A.; Morrisroe, E.; McCoey, J. M.; Lombard, A. H.; Mendis, D. C.; Treussart, F.; Hall, L. T.; Petrou, S.; Hollenberg, L. C. L. Non-Neurotoxic Nanodiamond Probes for Intraneuronal Temperature Mapping. *ACS Nano* **2017**, *11*, 12077.

(14) Fu, C.-C.; Lee, H.-Y.; Chen, K.; Lim, T.-S.; Wu, H.-Y.; Lin, P.-K.; Wei, P.-K.; Tsao, P.-H.; Chang, H.-C.; Fann, W. Characterization and Application of Single Fluorescent Nanodiamonds as Cellular Biomarkers. *Proc. Natl. Acad. Sci. U.S.A.* **2007**, *104*, 727−732.

(15) Tanimoto, R.; Hiraiwa, T.; Nakai, Y.; Shindo, Y.; Oka, K.; Hiroi, N.; Funahashi, A. Detection of Temperature Difference in Neuronal Cells. *Sci. Rep.* **2016**, *6*, 22071.

(16) Balasubramanian, G.; Lazariev, A.; Arumugam, S. R.; Duan, D.-w. Nitrogen-Vacancy color center in diamond-emerging nanoscale applications in bioimaging and biosensing. *Curr. Opin. Chem. Biol.* **2014**, *20*, 69−77.

(17) Tetienne, J.-P.; et al. The Nature of Domain Walls in Ultrathin Ferromagnets Revealed by Scanning Nanomagnetometry. *Nat. Commun.* **2015**, *6*, 6733.

(18) Grinolds, M. S.; Hong, S.; Maletinsky, P.; Luan, L.; Lukin, M. D.; Walsworth, R. L.; Yacoby, A. Nanoscale Magnetic Imaging of a Single Electron Spin under Ambient Conditions. *Nat. Phys.* **2013**, *9*, 215−219.

(19) Trusheim, M. E.; Li, L.; Laraoui, A.; Chen, E. H.; Bakhru, H.; Schröder, T.; Gaathon, O.; Meriles, C. A.; Englund, D. Scalable Fabrication of High Purity Diamond Nanocrystals with Long-Spin-Coherence Nitrogen Vacancy Centers. *Nano Lett.* **2014**, *14*, 32−36.

(20) Schirhagl, R.; Chang, K.; Loretz, M.; Degen, C. L. Nitrogen-Vacancy Centers in Diamond: Nanoscale Sensors for Physics and Biology. *Annu. Rev. Phys. Chem.* **2014**, *65*, 83−105.

(21) Karaveli, S.; Gaathon, O.; Wolcott, A.; Sakakibara, R.; Shemesh, O. A.; Peterka, D. S.; Boyden, E. S.; Owen, J. S.; Yuste, R.; Englund, D. Modulation of Nitrogen Vacancy Charge State and Fluorescence in Nanodiamonds Using Electrochemical Potential. *Proc. Natl. Acad. Sci. U.S.A.* **2016**, *113*, 3938−3943.

(22) Horowitz, V. R.; Alemán, B. J.; Christle, D. J.; Cleland, A. N.; Awschalom, D. D. Electron Spin Resonance of Nitrogen-Vacancy

Centers in Optically Trapped Nanodiamonds. *Proc. Natl. Acad. Sci. U.S.A.* **2012**, *109*, 13493.

(23) Mittiga, T.; Hsieh, S.; Zu, C.; Kobrin, B.; Machado, F.; Bhattacharyya, P.; Rui, N.; Jarmola, A.; Choi, S.; Budker, D.; Yao, N. Imaging the Local Charge Environment of Nitrogen-Vacancy Centers in Diamond. *Phys. Rev. Lett.* **2018**, *121*, 246402.

(24) Manson, N. B.; Harrison, J. P.; Sellars, M. J. Nitrogen-vacancy Center in Diamond: Model of the Electronic Structure and Associated Dynamics. *Phys. Rev. B: Condens. Matter Mater. Phys.* **2006**, *74*, 104303.

(25) Gruber, A.; Dräbenstedt, A.; Tietz, C.; Fleury, L.; Wrachtrup, J.; Von Borczyskowski, C. Scanning Confocal Optical Microscopy and Magnetic Resonance on Single Defect Centers. *Publ. Am. Assoc. Adv. Sci.* **1997**, *276*, 2012−2014.

(26) Brites, C. D. S.; Lima, P. P.; Silva, N. J. O.; Millán, A.; Amaral, V. S.; Palacio, F.; Carlos, L. D. Thermometry at the Nanoscale. *Nanoscale* **2012**, *4*, 4799−4829.

(27) Doherty, M. W.; Manson, N. B.; Delaney, P.; Jelezko, F.; Wrachtrup, J.; Hollenberg, L. C. L. The Nitrogen-Vacancy Colour Centre in Diamond. *Phys. Rep.* **2013**, *528*, 1.

(28) Acosta, V.; Bauch, E.; Ledbetter, M.; Waxman, A.; Bouchard, L.-S.; Budker, D. Temperature Dependence of the Nitrogen-Vacancy Magnetic Resonance in Diamond. *Phys. Rev. Lett.* **2010**, *104*, 070801.

(29) Taylor, J. M.; Cappellaro, P.; Childress, L.; Jiang, L.; Budker, D.; Hemmer, P. R.; Yacoby, A.; Walsworth, M. D.; Lukin, M. High-Sensitivity Diamond Magnetometer With Nanoscale Resolution. *Nat. Phys.* **2008**, *4*, 810−816.

(30) Rondin, L.; Tetienne, J. P.; Hingant, T.; Roch, J. F.; Maletinsky, P.; Jacques, V. Magnetometry with Nitrogen-vacancy Defects in Diamond. *Rep. Prog. Phys.* **2013**, *77*, 056503.

(31) Maertz, B.; Wijnheijmer, A.; Fuchs, G.; Nowakowski, M.; Awschalom, D. Vector Magnetic Field Microscopy Using Nitrogen Vacancy Centers in Diamond. *Appl. Phys. Lett.* **2010**, *96*, 092504.

(32) Wang, P.; Yuan, Z.; Huang, P.; Rong, X.; Wang, M.; Xu, X.; Duan, C.; Ju, C.; Shi, F.; Du, J. High-Resolution Vector Microwave Magnetometry Based on Solid-State Spins in Diamond. *Nat. Commun.* **2015**, *6*, 6631.

(33) Clevenson, H.; Pham, L. M.; Teale, C.; Johnson, K.; Englund, D.; Braje, D. Robust High-Dynamic-Range Vector Magnetometry With Nitrogen-Vacancy Centers in Diamond. *Appl. Phys. Lett.* **2018**, *112*, 252406.

(34) Schloss, J. M.; Barry, J. F.; Turner, M. J.; Walsworth, R. Simultaneous Broadband Vector Magnetometry Using Solid-State Spins. *Phys. Rev. Appl.* **2018**, *10*, 034044.

(35) Chen, E. H.; Gaathon, O.; Trusheim, M. E.; Englund, D. Wide-Field Multispectral Super-Resolution Imaging Using Spin-Dependent Fluorescence in Nanodiamonds. *Nano Lett.* **2013**, *13*, 2073−2077.

(36) Plakhotnik, T.; Doherty, M. W.; Cole, J. H.; Chapman, R.; Manson, N. B. All-Optical Thermometry and Thermal Properties of the Optically Detected Spin Resonances of the NV- Center in Nanodiamond. *Nano Lett.* **2014**, *14*, 4989−4996.

(37) Doherty, M. W.; Acosta, V. M.; Jarmola, A.; Barson, M. S. J.; Manson, N. B.; Budker, D.; Hollenberg, L. C. L. Temperature Shifts of the Resonances of the Nv- Center in Diamond. *Phys. Rev. B: Condens. Matter Mater. Phys.* **2014**, *90*, 041201.

(38) Nagl, A.; Hemelaar, S. R.; Schirhagl, R. Improving surface and defect center chemistry of fluorescent nanodiamonds for imaging purposes-a review. *Anal. Bioanal. Chem.* **2015**, *407*, 7521−7536.

(39) Tetienne, J.-P.; Lombard, A.; Simpson, D. A.; Ritchie, C.; Lu, J.; Mulvaney, P.; Hollenberg, L. C. L. Scanning Nanospin Ensemble Microscope for Nanoscale Magnetic and Thermal Imaging. *Nano Lett.* **2016**, *16*, 326−333.

(40) Andrich, P.; Li, J.; Liu, X.; Heremans, F. J.; Nealey, P. F.; Awschalom, D. D. Microscale-Resolution Thermal Mapping Using a Flexible Platform of Patterned Quantum Sensors. *Nano Lett.* **2018**, *18*, 4684−4690.

(41) Dong, H.; Wen, B.; Melnik, R. Relative Importance of Grain Boundaries and Size Effects in Thermal Conductivity of Nanocrystalline Materials. *Sci. Rep.* **2015**, *4*, 7037.

(42) Photron. TECHIMAGING, **2018**, https://www.techimaging.com/products/high-speed-cameras.

(43) Zanoni, E.; Meneghini, M.; Chini, A.; Marcon, D.; Meneghesso, G. AlGaN/GaN-Based HEMTs Failure Physics and Reliability: Mechanisms Affecting Gate Edge and Schottky Junction. *IEEE Trans. Electron Devices* **2013**, *60*, 3119−3131.

(44) Chowdhury, S.; Mishra, U. K. Lateral and Vertical Transistors Using the AlGaN/GaN Heterostructure. *IEEE Trans. Electron Devices* **2013**, *60*, 3060−3066.

(45) Bagnall, K. R.; Moore, E. A.; Badescu, S. C.; Zhang, L.; Wang, E. N. Simultaneous Measurement of Temperature, Stress, and Electric Field in Gan Hemts With Micro-Raman Spectroscopy. *Rev. Sci. Instrum.* **2017**, *88*, 113111.

(46) Kuball, M.; Hayes, J. M.; Uren, M. J.; Martin, I.; Birbeck, J. C. H.; Balmer, R. S.; Hughes, B. T. Measurement of Temperature in Active High-power AlGaN/GaN HFETs using Raman Spectroscopy. *IEEE Electron Device Lett.* **2002**, *23*, 7−9.

(47) Sarua, A.; Hangfeng Ji, H.; Kuball, M.; Uren, M. J.; Martin, T.; Hilton, K. P.; Balmer, R. S. Integrated micro-Raman/infrared thermography probe for monitoring of self-heating in AlGaN/GaN transistor structures. *IEEE Trans. Electron Devices* **2006**, *53*, 2438−2447.

(48) Kuball, M.; Pomeroy, J. W. A Review of Raman Thermography for Electronic and Opto-Electronic Device Measurement With Submicron Spatial and Nanosecond Temporal Resolution. *IEEE Trans. Device Mater. Reliab.* **2016**, *16*, 667−684.

(49) Balasubramanian, G.; Neumann, P.; Twitchen, D.; Markham, M.; Kolesov, R.; Mizuochi, N.; Isoya, J.; Achard, J.; Beck, J.; Tissler, J.; Jacques, V.; Hemmer, P. R.; Jelezko, F.; Wrachtrup, J. Ultralong Spin Coherence Time in Isotopically Engineered Diamond. *Nat. Mater.* **2009**, *8*, 383−387.